Lattice vibrations of γ- and β-coronene from Raman microscopy and theory

Nicola Bannister,[1] Jonathan Skelton,[2] Gabriele Kociok-Köhn,[3] Tim Batten,[4] Enrico Da Como,[1] and Simon Crampin[1]

[1]*Department of Physics, University of Bath, Claverton Down, Bath BA2 7AY, United Kingdom*

[2]*School of Chemistry, University of Manchester, Manchester M13 9PL, United Kingdom*

[3]*Department of Chemistry and Material and Chemical Characterisation Facility (MC²), University of Bath, Claverton Down, Bath BA2 7AY, United Kingdom*

[4]*Renishaw plc, Wotton-under-Edge, Gloucestershire GL12 7DW, United Kingdom*

We combine polarization-resolved low-frequency Raman microscopy and dispersion-corrected density-functional calculations (DFT-D3) to study polymorph-dependent lattice vibrations in coronene, a model molecular system for nanographenes and disklike organic semiconductors that exhibits two crystalline structures with distinct electronic and optical properties. Changes in low-energy Raman-active lattice phonons are followed across the γ- to β-phase transition at 150 K. Raman frequencies calculated using DFT-D3 agree to within 4 cm^{-1}, and on the basis of polarization dependence of peak positions and intensities we achieve a clear mode assignment. Studies of the associated atomic motions show how the pure librational and rotational modes of γ-coronene change into mixed roto-librations in the β-phase, explaining the remarkable differences in Raman spectra of the two phases.

I. INTRODUCTION

The lattice dynamics of molecular solids have a significant impact on their electronic and optical properties [1]. In technological applications, phonons influence charge transport in molecular semiconductors, ultimately limiting maximum carrier mobilities in organic electronic devices [2–5], and the performance of materials for thermoelectric applications [6]. More fundamentally, the vibrational spectrum contributes to the relative thermodynamic stability of crystalline structures [7], and it must be considered when attempting to explain polymorphism, the existence of different crystal structures for the same molecular compound [8]. Here we report a combined experiment and theory study of lattice vibrations in the two different polymorphs of the molecular crystal coronene.

Molecular crystals are held together by dispersive forces (van der Waals), which dominate intermolecular interactions, but they are far weaker than the strong intramolecular covalent bonds. As a consequence, the description of their structural, phononic, and electronic properties by *ab initio* density functional theory (DFT) methods remains challenging. Even the most recently developed exchange-correlation functionals do not describe dispersion, which is the fundamental interaction for the cohesive energy in these van der Waals solids [9]. Phenomenologically, the distinction between inter- and intramolecular interactions is usually reflected in the vibrational modes, allowing a classification into intermolecular phonons and intramolecular vibrational modes [10]. Although the distinction is not always well defined, as modes with mixed character can occur, phonons are typically observed at frequencies <200 cm^{-1}, while the spectrum at high frequencies is dominated by intramolecular modes. On account

of their origin being the intermolecular van der Waals interactions, it is the low-frequency modes that are most sensitive to variations in crystal structure, and able to be used as probes to test the validity of dispersion-corrected DFT methods [11]. Experimentally, they can be readily observed with low-frequency Raman spectroscopy, a technique that has also proven to be effective for studies of polymorphism in several condensed polyaromatic systems [8] as well as being used to estimate electron-phonon coupling in organic semiconductors [4,12], highlighting the importance of Raman for understanding charge transport in this fascinating class of materials [13]. Beyond molecular crystals, another class of van der Waals solids, the transition-metal chalcogenides, also exhibit a clear distinction between modes involving covalent and noncovalent bonds, and Raman spectroscopy of interlayer phonons has proven useful in studying polytypism and film thickness in few-layer systems [14–16].

The *ab initio* DFT-based description of molecular crystals using dispersion corrections has attracted substantial interest in recent years. This has been motivated by the design of theoretical tools aimed at predicting thermodynamic stability of polymorphic crystal structures, especially in connection with pharmaceuticals. Because of the intermolecular nature of low-frequency phonons, a correct theoretical description of such excitations is recognized as one of the most rigorous tests for any dispersion-corrected DFT model [11]. Additionally, the already mentioned role of phonons in determining the relative thermodynamic stability of different crystal structures points toward their correct description as the first step in any attempt to explain the complex scientific problem of polymorphism.

Among organic aromatic semiconductors such as pentacene, tetracene, perylene, and others that exhibit
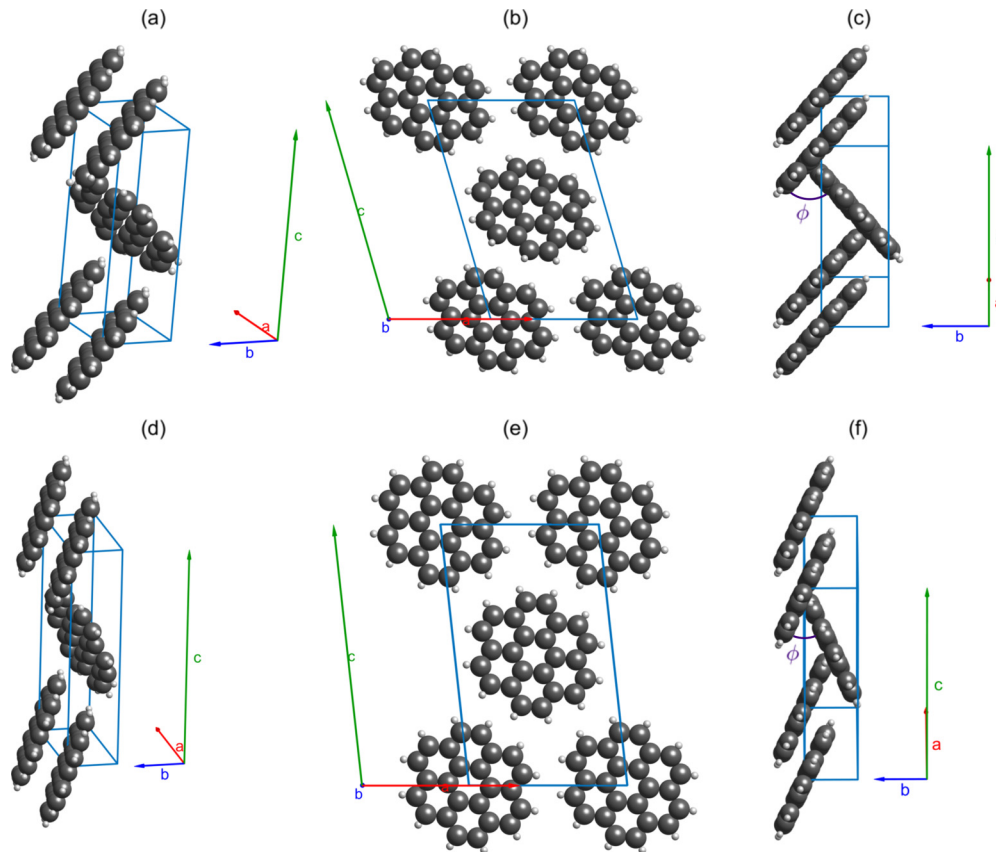
FIG. 1. Crystal structures of (a)–(c) γ- and (d)–(f) β-coronene obtained at 290 and 150 K, respectively. The γ-coronene structure was measured in this work using single-crystal x-ray diffraction while the β-coronene structure is taken from Ref. [26]. Clearly visible are the changes in the lengths of cell vectors $\vec{b}$ and $\vec{c}$, the decrease in the angle, β, between cell vectors $\vec{a}$ and $\vec{c}$, and the large change in the intracell molecular angle, ϕ, between the molecular planes of the two translationally inequivalent $C_{24}H_{12}$ molecules within the unit cell.

polymorphism, coronene has garnered much interest [17–21]. Several optical spectroscopy experiments have indicated structural phase transitions upon cooling single crystals [22–26] and also under pressure [23,27], and the existence of two stable crystalline structures has been reported [26]. Very recently, Salzillo *et al.* have reported high-quality low-wave-number Raman spectra of single crystals as a function of temperature, and modeled them using dispersion-corrected density-functional theory [28]. Upon cooling below $T \simeq 150$ K, the common phase, γ, transforms into a second phase, the β phase. Both phases contain two molecules per unit cell, but with a major difference in the angle between the molecular planes [Figs. 1(c) and 1(f)]. In this work, we use low-frequency Raman spectroscopy and the dispersion-corrected density-functional theory model DFT-D3 to study the Raman spectrum across the phase transition, assigning the spectra and establishing the key differences between the polymorphs. We consider this as the first step toward the identification of an adequate *ab initio* model for the description of phonons and future discussions on their roles in the phase transition. We identify the Raman-active phonons of γ-coronene as rotations and librations of the molecules with axes almost perpendicular and parallel to the plane of π bonds, respectively. In β-coronene, the axes of rotation and libration are instead at intermediate angles with respect to the molecular plane and result in modes

that appear to be combinations of librations and rotations. We also explain the correlation between the geometrical characteristics of the modes and the Raman activity.

II. METHODS

A. Computations

Energy calculations and structural optimizations were performed using the Vienna *ab initio* simulation package (VASP) code [29]. The Perdew-Burke-Ernzerhof (PBE) functional [30] was employed with projector augmented wave (PAW) pseudopotentials [31,32] and a kinetic energy cutoff of 850 eV for the plane-wave basis. The Grimme-D3 scheme [33,34] was used to account for van der Waals forces. For both structures, a Γ-centered $2 \times 3 \times 1$ Monkhorst-Pack k-point mesh was used to sample the Brillouin zone. Increasing k-point sampling to $3 \times 4 \times 2$, as used in previous work [26], gave a difference in the lattice energies of 3 meV and a <0.3% change in unit-cell parameters. Total-energy calculations were considered converged when the energy change between two successive electronic steps was less than 10^{-8} eV. Structures were allowed to fully relax until all forces acting on the atoms were <10^{-4} eV/Å. Phonopy [35,36] was used to calculate vibrational frequencies and eigenvectors within the harmonic approximation. VASP was used as the force calculator with a finite displacement step of 0.015 Å. Raman

activity tensors were calculated using a central-differences scheme [37–39] with required dielectric constants calculated using VASP. The symmetry labels of vibrational modes were output by Phonopy from in-built group tables.

B. Crystal growth

Crystals of γ-coronene were grown using a physical transport method in a three-zone furnace [40]. Powdered γ-coronene crystals of 97% purity were sourced from Sigma-Aldrich and twice purified by sublimation under vacuum. The purified γ-coronene was placed on a platform in a quartz boat at one end of a quartz tube inside the furnace. The furnace was heated to 175, 225, and 275 °C at the end, middle and sample end, respectively. Gaseous argon was set to flow from hot to cold at a rate of approximately 40 cm^{-3}/min. After 2 days the furnace was allowed to cool, and crystals were removed. The two purification steps were found to be critical in reducing the fluorescence background in Raman experiments enabling better resolution of the peaks—the origin of the residual fluorescence is unknown but could be linked to a defect-enhanced two-photon absorption process as recently observed in rubrene [41]. Crystals of β-coronene were obtained by cooling the purified γ-coronene crystals below 150 K.

C. Single-crystal x-ray diffraction

Data collection was carried out at four different temperatures, starting at 290 K, decreasing to 200 K at 300 K/h and stabilizing for 2 min, then further decreasing to 150 and 80 K with a stabilizing time of 10 min. Diffraction datasets were collected on a Rigaku SuperNova, Dual, Cu at zero, EosS2 single-crystal diffractometer using monochromated Cu $K\alpha$ radiation with $\lambda = 1.541\,84$ Å. A symmetry-related (multiscan) absorption correction was applied with CrysAlisPro 1.171.38.43. Structures were solved with SHELXT and refined by full-matrix least-squares fits on F^2 [42], with additional analysis performed using SHELXle [43]. We found that the crystals deteriorated at 80 K, preventing further characterization.

D. Raman

Raman measurements were performed using a Renishaw InVia Raman spectrometer operated in backscatter geometry, equipped with a 633 nm excitation laser, 2400 lines/mm grating, and a long working distance 50× objective lens (NA = 0.5). The spectral resolution of this configuration was better than 1 cm^{-1}. Volume Bragg grating notch filters (Eclipse) with a nominal cutoff of ± 10 cm^{-1} were used to measure the low-frequency Raman modes. The laser power incident on the sample was 4.0 ± 0.1 mW. To control the temperature during measurements, the sample was placed in a Linkam THMS600 stage and Raman measurements were collected through a quartz window, reducing the laser power to 3.7 ± 0.1 mW. The stage has an operational temperature range of 77 to 327 K and an accuracy of the order 0.1 K. For polarization measurements, a rotatable $\lambda/2$ waveplate, with an accuracy of <1° on rotated angle between 0° and 90°, was placed in the path of the laser before the sample, and a linear polarizer was placed after the sample and in front of the detector. Peaks were

fit using Voigt profiles [44–46] to account for the intrinsic Lorentzian line shapes and Gaussian broadening imposed by the instrumentation [47].

III. RESULTS AND DISCUSSION

We first compare the crystal structures of the two phases predicted from our DFT-D3 calculations to experimental measurements. We then present a comprehensive characterisation of the low-frequency Raman spectra across the phase transition. Initial mode assignments are made based on peak positions and confirmed by measuring the polarization dependence of the Raman activity. Finally, the differences in spectra of the two polymorphs is rationalised by analyzing the atomic motion associated with the vibrations.

A. Crystal structures

A series of single-crystal x-ray diffraction measurements were taken on a γ-coronene crystal; see Fig. 2. The lattice parameters show a linear temperature dependence, which produces extrapolated 0 K values of $a = 9.98$ Å, $b = 4.65$ Å, $c = 15.50$ Å, and $\beta = 106.82°$ giving a volume $V = 688$ Å^3 and an intracell molecular angle, as indicated in Fig. 1(c), of $\phi = 86.83°$.

Starting from the experimental γ-coronene structure, relaxation with DFT-D3 yields lattice parameters $a = 9.98$ Å, $b = 4.76$ Å, $c = 15.42$ Å, and $\beta = 106.38°$ giving $V = 703$ Å^3. The intracell molecular angle is $\phi = 85.96°$. As seen in Figs. 2(b) and 2(c), the main differences between the calculated and measured structures are a larger b-axis and a slightly smaller c-axis. These are within 1.6% of the lattice parameters measured at 290 K and within 2.5% of the extrapolated 0 K values, while ϕ is within 0.7% of the 290 K value and 1.0% of the 0 K extrapolation, indicating that our relaxed γ-coronene crystal structure is comparable to experiment. The level of agreement gives confidence in using DFT-D3 to interpret our experimental results.

The β phase was also optimized using DFT-D3. Relaxations starting from experimental lattice parameters and previously reported DFT results [26] both produced identical final structures. The calculated lattice parameters are $a = 10.31$ Å, $b = 3.92$ Å, $c = 17.17$ Å, and $\beta = 96.05°$ giving $V = 690$ Å^3, with an intracell molecular angle of $\phi = 49.86°$. Figure 2 shows a comparison between our DFT-D3 lattice parameters and the measured parameters in Ref. [26]. The largest differences with experimental measurements are a decrease in the predicted a-axis and an increase in the b-axis [Figs. 2(a) and 2(b)]. Our lattice parameters are within 2.1% of those measured at 150 K and within 3.1% of the extrapolated 0 K values. The intracell molecular angle is within 0.4% at 150 K and 1.1% of the 0 K extrapolation. This again indicates that DFT-D3 is appropriate for further calculations.

B. Raman

Figure 3(a) shows Raman spectra recorded from a single γ-coronene crystal while reducing the temperature at a rate of 15 K/min. Between 300 and 175 K, two peaks labeled A and B are visible, as observed in previous Raman measurements
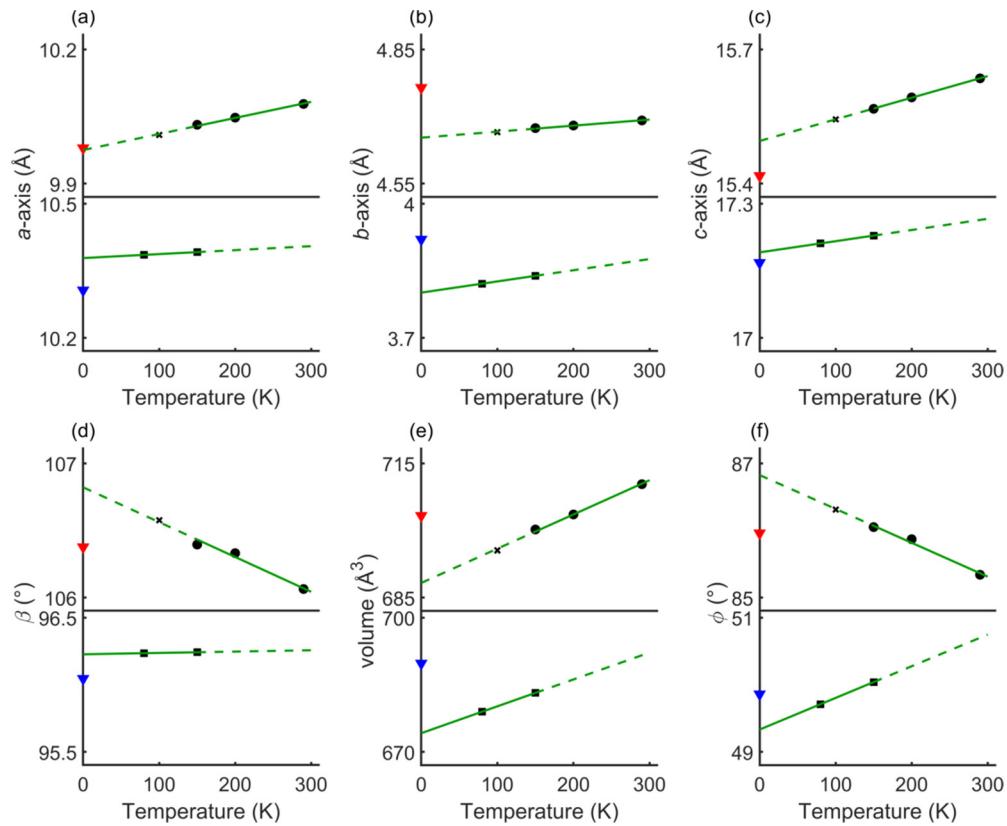
FIG. 2. Temperature dependence of (a)–(c) lattice parameters, (d) cell angle β, (e) cell volume, and (f) intracell molecular angle ϕ. Top panels show γ-coronene and bottom panels β-coronene. Red and blue triangles are from our DFT-D3 calculations for γ- and β-coronene, respectively. Black circles show our measurements from single-crystal x-ray diffraction, black $\times$ show data from Ref. [48], and black squares are from Ref. [26]. Green lines show the fitted linear trend lines.
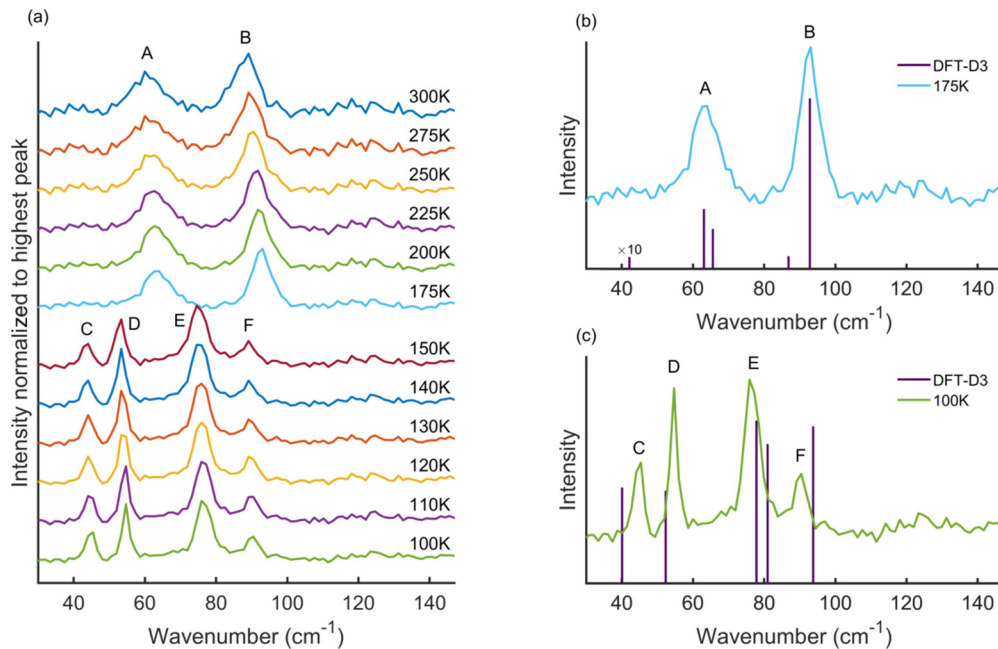

FIG. 3. (a) Raman spectra collected from a single γ-coronene crystal during a temperature sweep from 300 to 100 K. The crystal was observed to shatter at 163 K, corresponding to the striking change in spectral shape. For each spectrum, background envelopes have been removed and intensities normalized to the highest peak. Individual spectra are offset for clarity. Parts (b) and (c) compare Raman spectra in the two temperature regimes to orientationally averaged (powder) Raman intensities calculated using DFT-D3 for γ- and β-coronene, respectively.

TABLE I. Raman frequencies and intensities fitted from experimental spectra and from DFT-D3 calculations on γ-coronene. Modes 3 and 4 overlap in experiment due to their similar frequencies and line broadening effects producing peak A.

Mode ID	175 K experiment		DFT-D3	
	Frequency (cm^{-1})	Intensity (k counts)	Frequency (cm^{-1})	Intensity ($\text{\AA}^4$ amu^{-1})
1	not observed		34.13	0.2
2	not observed		42.15	2.4
3	(A) 63.5	21.4	63.09	125.0
4			65.60	82.9
5	not observed		86.85	25.3
6	(B) 92.8	47.6	92.85	359.7

TABLE II. Raman frequencies and intensities fitted from experimental spectra and from DFT-D3 calculations on β-coronene. Peak E was fitted with two-component Voigt profiles giving E_1 and E_2.

Mode ID	100 K experiment		DFT-D3	
	Frequency (cm^{-1})	Intensity (kcounts)	Frequency (cm^{-1})	Intensity ($\text{\AA}^4$ amu^{-1})
1	not observed		17.73	0.7
2	(C) 44.8	10.2	40.10	60.4
3	(D) 54.6	24.0	52.34	58.3
4	(E_1) 76.6	20.7	77.84	102.9
5	(E_2) 77.5	4.6	80.97	88.0
6	(F) 90.3	8.1	93.77	99.3

[22,28]. At 163 K the crystal was observed to shatter. Subsequent spectra recorded from a crystal fragment between 150 and 100 K show four peaks labeled C–F. It has recently been confirmed from x-ray experiments that a phase transition occurs at $\sim$150 K and the low-temperature phase was determined to be the β phase of coronene [26,49]. A second crystal fragment measured while increasing temperature gave consistent results [50]. In both phases, as the temperature decreases, the peaks shift to higher frequencies.

For γ-coronene, the calculations predict six Raman-active modes (Table I). These are compared with the experimental spectra in Fig. 3(b). The two lowest frequency modes at 34.13 cm^{-1} (mode 1) and 42.15 cm^{-1} (mode 2) are predicted to have very small intensities in comparison to the other four, which is consistent with these two modes being absent in the experimental spectra. Of the other modes, the first two are close in frequency [63.09 cm^{-1} (mode 3) and 65.60 cm^{-1} (mode 4)] and have similar intensities, such that line broadening causes the modes to overlap and produce peak A at 63.5 cm^{-1} in the experimental spectra. Mode 5 (86.85 cm^{-1}) is unlikely to be observed, as mode 6 (92.85 cm^{-1}) has >14 times higher intensity, making it hard to discern mode 5 above the background and/or the tail of mode 6. We note that the predicted intensities assume an orientational average of the Raman activity tensors, which means a quantitative comparison of the intensity profiles is not realistic given that the experiments were performed on a single crystal of unknown orientation, which will create a spatial dependence of the intensity. Despite this, however, the peak positions agree well, enabling a tentative mode assignment to be made.

For β-coronene, DFT-D3 again predicts six Raman-active modes (Table II), which are compared to the experimental spectra in Fig. 3(c). The lowest-frequency mode at 17.73 cm^{-1} (mode 1) is not observed in our experiments, due both to its low intensity and the frequency lying below our realistic analysis window of >30 cm^{-1} due to noise from other sources of scattering. Of the remaining five modes, Fig. 3(c) suggests that the two modes at 77.84 cm^{-1} (mode 4) and 80.97 cm^{-1} (mode 5) overlap in the experiments to produce peak E. The other three modes predicted at 40.10 cm^{-1} (mode 2), 52.34 cm^{-1} (mode 3), and 93.77 cm^{-1} (mode 5) can be individually resolved in the spectra. By fitting the experimental spectra with five Voigt profiles, peak E can be deconvoluted into two

component peaks at 76.6 cm^{-1} (E_1) and 77.5 cm^{-1} (E_2). The other three peaks, C, D, and F, occur at 44.8, 54.6, and 90.3 cm^{-1}, respectively. Small discrepancies of up to 4 cm^{-1} in frequency between the experimental and predicted frequencies are observed, which we ascribe to a combination of small disparities in the predicted crystal structure, anharmonicity, and thermal effects.

To further confirm the assignment of modes, the full Raman tensors were calculated from DFT-D3 and used to simulate polarized Raman measurements, which are compared to experimental measurements in Figs. 4(a) and 4(b).

For γ-coronene, as the input polarization is rotated from $0°$ to $90°$, the intensity of the A and B peaks decreases until they are unobservable above the noise level at $90°$, and then increases again to a maximum at $180°$. Neither of the peak positions changes with polarization, indicating that both have a single component, and thus both peaks were fitted to a single Voigt profile. All the polarized spectra were fitted simultaneously, with the peak positions and the Gaussian and Lorentzian widths constrained to be the same. The peak positions fitted here are lower in frequency than those listed in Table I as the polarization measurements were performed at room temperature [cf. Fig. 3(a)]. Intensity as a function of input polarization angle is shown in Fig. 4(c), and half figure-of-eight shapes were observed for both peaks.

To interpret these results using our calculations, it was necessary to determine the orientation of the crystal sample, so face indexing was carried out using x-ray diffraction [50]. The long crystal side, determined to be the b-axis, was aligned with the experimental vertical at $0°$. With this knowledge, the Raman intensity as a function of input polarization was calculated using the Raman tensors [Fig. 4(c); for ease of analysis, modes 3 and 4 of γ-coronene were combined]. The combined intensity polar plot for modes 3 and 4 results in an oval shape, since both modes exhibit figure-of-eight behavior but with lobes at $90°$ to each other. Mode 6 also exhibits figure-of-eight behavior, with lobes at $0°$ and $180°$. Mode 5 was excluded from the analysis as it is not resolved in the experimental measurements, and combining it with mode 6 when analyzing the calculation results was found to make an insignificant difference to the predicted polar plot. Our calculations correctly predict the polarization dependence of the intensities of all of the peaks, confirming our mode assignments. A second set of measurements was also performed
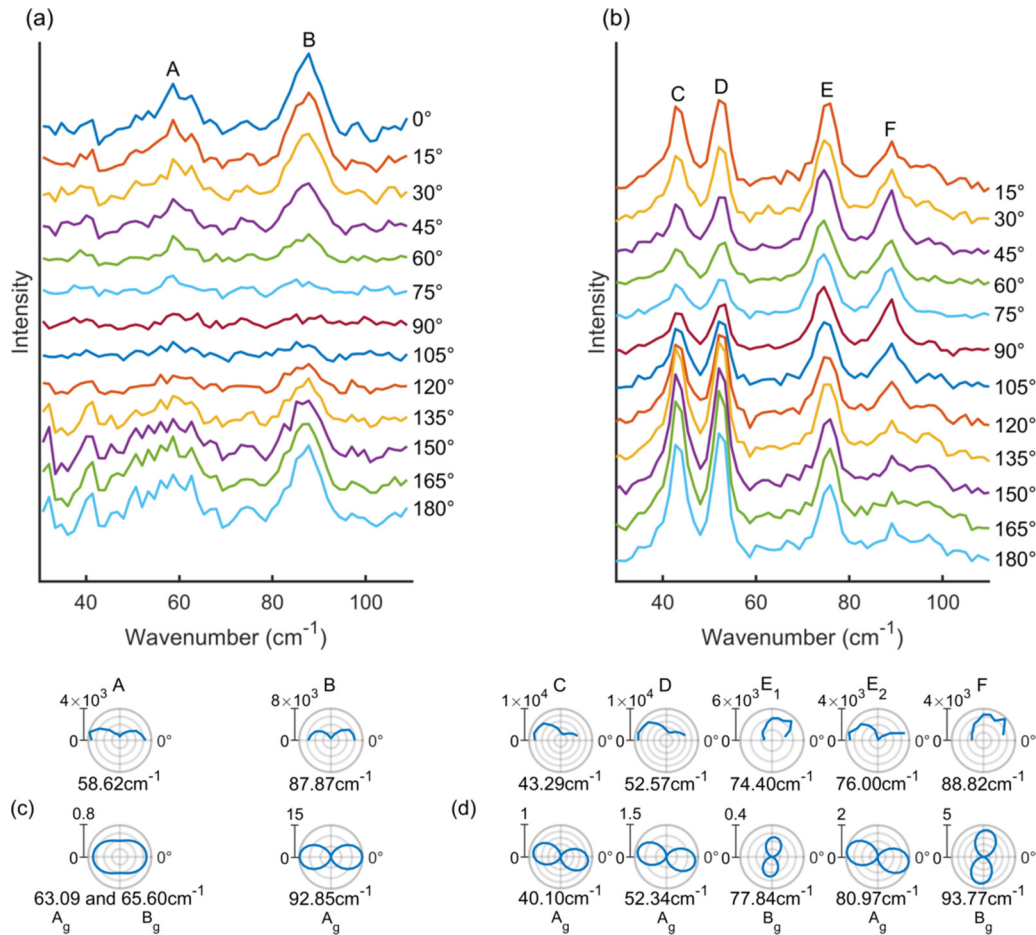
FIG. 4. Polarization angle dependence of Raman spectra for (a) γ- and (b) β-coronene, respectively. Individual spectra are offset for clarity. The peak intensity as a function of polarization angle for (c) γ- and (d) β-coronene. The top rows show profiles extracted by fitting the experimental spectra, while the bottom rows show the profiles predicted from our calculations. The $0°$ measurements for β-coronene have been excluded due to anomalies arising from local heating by the laser.

with the output polarizer rotated by $90°$ [50]—in these measurements, peak A was suppressed in intensity, meaning no useful data could be extracted, while the calculations again predicted the correct polarization dependence of the intensity of peak B, further confirming our mode assignments.

Low-temperature polarization measurements on the β-coronene phase were also carried out [Fig. 4(b)]. The positions of peaks C, D, and F exhibit no polarization dependence, while the position of peak E shifts slightly as the input polarization is varied, which confirms that peak E is indeed a combination of multiple modes, consistent with our earlier assignment [Fig. 3(c)]. The spectra were fitted to a set of five Voigt functions using the method detailed above. All five modes showed figure-of-eight dependencies on the polarization [Fig. 4(d)]. Peaks C, D, and E_2 show half figure of eights with lobes at $\sim 0°$ and $\sim 180°$, while peaks E_1 and F show only one lobe at $\sim 90°$. Note that the figures of eight are slightly rotated from $0°$ and $90°$, which is due to the long side of the crystal fragment—assumed to be along the b-axis—being $8°$ away from the vertical ($0°$) in the experiments [50].

Since it was not possible to preserve the β-crystal fragment for face indexing, we generated polar plots from our calculations assuming the same face indexation as γ-coronene—both

structures are very similar, and will therefore very likely have similar preferred crystal faces. The predicted intensity polar plots, accounting for the $8°$ offset, are shown in Fig. 4(d), and again demonstrate very good agreement with our experiments. We find that the calculations again predict the correct polarization dependences, providing a clear assignment of modes.

Results with the detector polarization rotated by $90°$ are presented in [50]. These again show four peaks, which we fitted to five Voigt profiles, and the polarization dependence of the intensities again shows good agreement with our simulations.

C. Atomic motion

The preceding results indicate that there are remarkable differences in Raman spectra of γ- and β-coronene despite their very similar structures. To understand this difference, we compared the atomic motion associated with the vibrations of the two polymorphs predicted by the calculations.

The vibrational motion associated with the Raman-active phonon modes of both polymorphs is shown in Fig. 5. All of the modes involve rocking-type rotations of the molecules around an axis indicated by purple lines, which makes an
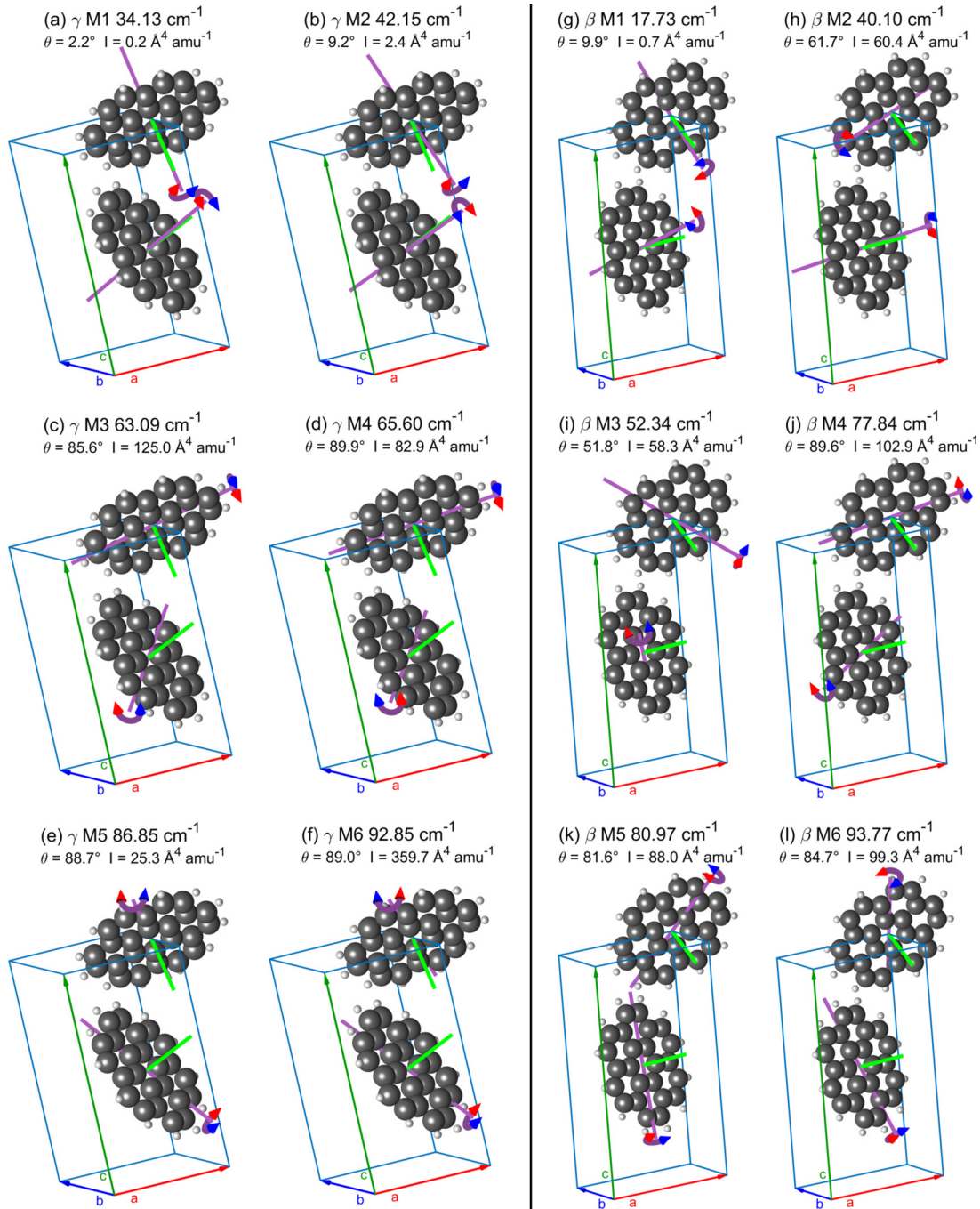
FIG. 5. Atomic motions associated with the Raman-active phonon modes in (a)–(f) γ- and (g)–(l) β-coronene. The frequency, the angle between the molecule normal and the axis of rotation, θ, and orientationally averaged Raman intensity, I, are given for each mode. Each illustration shows the motion of the two symmetrically inequivalent coronene molecules. The normal to the plane of each molecule is shown by a green line. The axis of rotation is shown with a purple line, and the direction of the rocking motion is shown by a purple arrow with a red and blue head. In any given plot, both molecules rotate in the same color direction at any instant.

angle θ to the normal of the molecular plane (the molecular normal axis) shown in green.

For γ-coronene, the six Raman-active modes can be grouped into sets of two. In the lowest-frequency pair, modes 1 and 2, the rotational axis is close to the molecular normal at $\theta = 2.2°$ and $9.2°$, respectively, indicating them to be rotational modes [Figs. 5(a) and 5(b)]. The difference between the molecular motions in the two modes is a reversal in the direction of one of the molecules. Since a molecule rotating

exactly around its molecular normal will not produce any significant change in polarization, the small angle θ away from the normal in these modes will result in a small change in polarization, explaining the small intensities calculated for these modes and the fact that these peaks were not seen in our measured Raman spectra.

Modes 3–6 all have rotational axes that are almost perpendicular to the molecular normal and are therefore predominantly librations. Each rocking rotation of a molecule will

produce a significant change in polarization, accounting for the higher intensities for these modes compared to modes 1 and 2. Modes 3 and 4 both rock around similar axes but with one molecule rotating in the opposite direction relative to the other mode [Figs. 5(c) and 5(d)]. Mode 3 has a higher intensity than mode 4, which can be explained by considering the contribution each molecule makes to the total change in polarization and the effect the reversal of one rotation direction has: one can think of a "constructive" addition of the change in polarization from each molecule in mode 3 producing a larger change in polarization, and hence intensity, while in mode 4 a "destructive"-like addition occurs producing a smaller change in polarization and a lower intensity. Modes 5 and 6 exhibit similar behavior [Figs. 5(e) and 5(f)], albeit with a significantly larger difference in the intensities. We speculate this is due to the rotational axes of the molecules in modes 5 and 6 being more in line with each other than in modes 3 and 4, giving a stronger "constructive/destructive" effect and hence intensity difference.

Turning to β-coronene, we find that the vibrational motions are markedly different, although some similarities can be observed. The lowest-frequency mode 1 is similar to that in γ-coronene in that the rotational axis is close to the molecular normal such that the mode corresponds to a rotation-type vibration with a low intensity, and the directions of rotation of the molecules are similar. In contrast, modes 2 and 3 show fundamentally different motion from any of the modes in γ-coronene. An angle θ of 61.7° and 51.8°, respectively, produces a change in polarization large enough to be observed experimentally, and indicates a mix of rotational and librational motion.

Modes 4–6 have rotational axes close to perpendicular to the normal axes, i.e., they have librational character, but they do not couple together like in γ-coronene, with all the rotational axes in different directions. With respect to the molecule, mode 4 has similar orientation and rotation directions to the corresponding mode 4 in γ-coronene, whereas mode 5 has no obvious pair and mode 6 is similar to mode 5 in γ-coronene. All three of these modes give measurable intensities and none dominates over the others. Hence five modes (2–6) in the four peaks C–F, where peak E is deconvoluted into two peaks by fitting, are observed in our experimental spectra.

IV. CONCLUSION

The lattice vibrations of γ- and β-coronene have been investigated using low-frequency Raman measurements and

the remarkable differences, given the similarity of the two polymorphs, rationalized with reference to the atomic motions predicted by DFT-D3 calculations. For γ- (β-) coronene, the calculations yield optimized structures with lattice parameters within 1.6% (2.1%) and an intracell angle within 0.7% (0.4%) of x-ray structures collected at 290 K (150 K) on single crystals. For both structures, the calculations predict six Raman-active phonon modes below 150 cm^{-1}, but taking into account differences in intensities and allowing for experimental resolution and a low wave number cutoff of 30 cm^{-1}, these are consistent with the two (four) peaks observed in Raman spectra taken from γ- (β-) coronene crystals, respectively, and which reflect contributions from three (five) modes with measured and calculated frequencies differing at most by 4 cm^{-1}.

The Raman spectra are consistent with the atomic motion predicted by the calculations. In γ-coronene, the modes are considered to be coupled into three pairs, with the lowest-frequency pair consistent with rotational motion giving rise to small intensities, and the remaining two pairs showing librational motion. In each pair, the axes of rotation were similar but with a reversal of direction of one molecule. In β-coronene, the lowest-frequency mode was found to be mostly rotational in character, and the three highest-frequency Raman-active phonon modes were mainly librational. The remaining two modes exhibit a mixture of rotational and librational behavior, with an angle between the rotational axis and molecular normal of ∼50°–60°. The excellent agreement between theory and experiment presented here justifies the study of lattice vibrations throughout the Brillouin zone using DFT-D3, a necessary step toward the understanding of phase stability and the phase transition. Both aspects will be reported on elsewhere.

[1] M. Schwoerer and H. C. Wolf, *Organic Molecular Solids* (Wiley, Weinheim, Germany, 2007).

[2] T. F. Harrelson, V. Dantanarayana, X. Xie, C. Koshnick, D. Nai, R. Fair, S. A. Nuñez, A. K. Thomas, T. L. Murrey, M. A. Hickner, J. K. Grey, J. E. Anthony, E. F. Gomez, A. Troisi, R. Faller, and A. J. Moulé, Mater. Horizons **6**, 182 (2019).

[3] S. Fratini, S. Ciuchi, D. Mayou, G. T. de Laissardière, and A. Troisi, Nat. Mater. **16**, 998 (2017).

[4] A. Y. Sosorev, D. Maslennikov, I. Y. Chernyshov, D. Dominskiy, V. Bruevich, M. Vener, and D. Y. Paraschuk, Phys. Chem. Chem. Phys. **20**, 18912 (2018).

[5] M. Ando, M. Yoneya, T. B. Kehoe, H. Ishii, T. Minakata, M. Kawasaki, C. M. Duffy, R. Phillips, and H. Sirringhaus, Phys. Rev. Mater. **3**, 025601 (2019).

[6] L. Cigarini, A. Ruini, A. Catellani, and A. Calzolari, J. Phys. D **50**, 395502 (2017).

[7] R. G. Della Valle, E. Venuti, and A. Brillante, Chem. Phys. **202**, 231 (1996).

[8] A. Brillante, I. Bilotti, R. G. Della Valle, E. Venuti, and A. Girlando, CrystEngComm **10**, 937 (2008).

[9] L. Kronik and A. Tkatchenko, Acc. Chem. Res. **47**, 3208 (2014).

[10] S. Califano, V. Schettino, and N. Neto, *Lattice Dynamics of Molecular Crystals* (Springer, Berlin, Heidelberg, 1981).

[11] S. Hirata, K. Gilliard, X. He, J. Li, and O. Sode, Acc. Chem. Res. **47**, 2721 (2014).

[12] M. Anderson, C. Ramanan, C. Fontanesi, A. Frick, S. Surana, D. Cheyns, M. Furno, T. Keller, S. Allard, U. Scherf, D. Beljonne, G. D'Avino, E. von Hauff, and E. Da Como, Phys. Rev. Mater. **1**, 055604 (2017).

[13] A. Girlando, L. Grisanti, M. Masino, I. Bilotti, A. Brillante, R. G. Della Valle, and E. Venuti, Phys. Rev. B **82**, 035208 (2010).

[14] J.-U. Lee, K. Kim, S. Han, G. H. Ryu, Z. Lee, and H. Cheong, ACS nano **10**, 1948 (2016).

[15] G. Froehlicher, E. Lorchat, F. Fernique, C. Joshi, A. Molina-Sánchez, L. Wirtz, and S. Berciaud, Nano Lett. **15**, 6481 (2015).

[16] D. L. Duong, G. Ryu, A. Hoyer, C. Lin, M. Burghard, and K. Kern, ACS Nano **11**, 1034 (2017).

[17] Y. Zhao and D. G. Truhlar, J. Phys. Chem. C **112**, 4061 (2008).

[18] H. Ruuska and T. A. Pakkanen, J. Phys. Chem. B **105**, 9541 (2001).

[19] S. Blumstengel, S. Sadofev, and F. Henneberger, New J. Phys. **10**, 065010 (2008).

[20] S. R. Langhoff, J. Phys. Chem. **100**, 2819 (1996).

[21] Y. Kubozono, H. Mitamura, X. Lee, X. He, Y. Yamanari, Y. Takahashi, Y. Suzuki, Y. Kaji, R. Eguchi, K. Akaike, T. Kambe, H. Okamoto, A. Fujiwara, T. Kato, T. Kosugi, and H. Aogi, Phys. Chem. Chem. Phys. **13**, 16476 (2011).

[22] K. Ohno, T. Kajiwara, and H. Inokuchi, Bull. Chem. Soc. Jpn. **45**, 996 (1972).

[23] T. Yamamoto, S. Nakatani, T. Nakamura, K.-i. Mizuno, A. H. Matsui, Y. Akahama, and H. Kawamura, Chem. Phys. **184**, 247 (1994).

[24] S. Nakatani, T. Nakamura, K. Mizuno, and A. Matsui, J. Lumin. **58**, 343 (1994).

[25] A. M. Orendt, J. C. Facelli, S. Bai, A. Rai, M. Gossett, L. T. Scott, J. Boerio-Goates, R. J. Pugmire, and D. M. Grant, J. Phys. Chem. A **104**, 149 (2000).

[26] J. Potticary, L. R. Terry, C. Bell, A. N. Papanikolopoulos, P. C. Christianen, H. Engelkamp, A. M. Collins, C. Fontanesi, G. Kociok-Köhn, S. Crampin, E. Da Como, and S. R. Hall, Nat. Commun. **7**, 11555 (2016).

[27] X.-M. Zhao, J. Zhang, A. Berlie, Z.-X. Qin, Q.-W. Huang, S. Jiang, J.-B. Zhang, L.-Y. Tang, J. Liu, C. Zhang, G.-H. Zhong, H.-Q. Lin, and C. Xiao-Jia, J. Chem. Phys. **139**, 144308 (2013).

[28] T. Salzillo, A. Giunchi, M. Masino, N. Bedoya-Martínez, R. G. Della Valle, A. Brillante, A. Girlando, and E. Venuti, Cryst. Growth Des. **18**, 4869 (2018).

[29] G. Kresse and J. Hafner, Phys. Rev. B **47**, 558 (1993).

[30] J. P. Perdew, K. Burke, and M. Ernzerhof, Phys. Rev. Lett. **77**, 3865 (1996).

[31] P. E. Blöchl, Phys. Rev. B **50**, 17953 (1994).

[32] G. Kresse and D. Joubert, Phys. Rev. B **59**, 1758 (1999).

[33] S. Grimme, Wiley Interdiscip. Rev. Comput. Mol. Sci. **1**, 211 (2011).

[34] S. Grimme, J. Antony, S. Ehrlich, and H. Krieg, J. Chem. Phys. **132**, 154104 (2010).

[35] A. Togo, F. Oba, and I. Tanaka, Phys. Rev. B **78**, 134106 (2008).

[36] A. Togo and I. Tanaka, Scr. Mater. **108**, 1 (2015).

[37] A. Fonari and S. Stauffer, vasp_raman.py, https://github.com/raman-sc/VASP.

[38] J. M. Skelton, L. A. Burton, A. J. Jackson, F. Oba, S. C. Parker, and A. Walsh, Phys. Chem. Chem. Phys. **19**, 12452 (2017).

[39] J. Skelton, Phonopy-Spectroscopy, https://github.com/JMSkelton/Phonopy-Spectroscopy.

[40] J. Henderson, M. Masino, L. E. Hatcher, G. Kociok-Köhn, T. Salzillo, A. Brillante, P. R. Raithby, A. Girlando, and E. Da Como, Cryst. Growth Des. **18**, 2003 (2018).

[41] C. D. Cruz, H. H. Choi, V. Podzorov, E. L. Chronister, and C. J. Bardeen, J. Phys. Chem. C **122**, 17632 (2018).

[42] G. M. Sheldrick, Acta Crystallogr. C **71**, 3 (2015).

[43] C. B. Hübschle, G. M. Sheldrick, and B. Dittrich, J. Appl. Crystallogr. **44**, 1281 (2011).

[44] R. Wells, J. Quant. Spectrosc. Radiat. Transf. **62**, 29 (1999).

[45] S. M. Abrarov and B. M. Quine, Appl. Math. Comput. **218**, 1894 (2011).

[46] W. Gautschi, SIAM J. Numer. Anal. **7**, 187 (1970).

[47] R. J. Meier, Vib. Spectrosc. **39**, 266 (2005).

[48] O. Kataeva, M. Khrizanforov, Y. Budnikova, D. Islamov, T. Burganov, A. Vandyukov, K. Lyssenko, B. Mahns, M. Nohr, S. Hampel, and M. Knupfer, Cryst. Growth Des. **16**, 331 (2015).

[49] J. Potticary, R. Boston, L. Vella-Zarb, A. Few, C. Bell, and S. R. Hall, Sci. Rep. **6**, 38696 (2016).

[50] See Supplemental Material at http://link.aps.org/supplemental/10.1103/PhysRevMaterials.3.125601 for full list of calculated phonon modes, additional Raman measurements with temperature dependence and with polarizer in detection rotated by 90°, and crystal face indexing.